PHYSICAL REVIEW FLUIDS **4**, 044604 (2019)

Effect of a bottom gap on the mean flow and turbulence structure past vertical solid and porous plates situated in the vicinity of a horizontal channel bed

K. Basnet and G. Constantinescu
Civil & Environmental Engineering Department & IIHR-Hydroscience and Engineering, The University of Iowa, Iowa City, Iowa 52242, USA

(Received 20 September 2018; published 10 April 2019)

The paper analyzes how the structure of the flow past solid (porosity $P = 0\%$) and porous ($P = 36\%$) plates containing parallel solid elements changes with increasing gap distance from the bottom surface. Fully three-dimensional large-eddy simulations are conducted in a straight channel with a horizontal smooth bottom surface and a vertical thin plate of height H positioned at a distance G from the channel bottom for $0 \leqslant G/H \leqslant 1$. For small G/H values, the main features of the wake flow are the formation of a bottom-attached recirculation region behind the plate and of corotating vortices originating from eddies shed inside the separated shear layer at the top edge of the plate. For sufficiently high G/H values, the wake flow is dominated by the shedding of counter-rotating wake vortices behind the plate (antisymmetric vortex shedding). For $G/H \leqslant 1$, the wake vortices originating in the bottom separated shear layer lose their coherence after they start interacting with the bottom surface. The effects of increasing G/H on the turbulent kinetic energy, nondimensional streamwise drag force acting on the plate and friction velocity distributions on the bottom surface are analyzed. The paper also discusses how the bleeding flow present in the porous plate cases affects the dynamics of the large-scale coherent structures and its effect on the spectral content of the flow, streamwise drag force, and bed friction velocity distributions.

DOI: 10.1103/PhysRevFluids.4.044604

I. INTRODUCTION

Placing a vertically oriented, solid or porous plate close to a horizontal bottom surface induces regions of flow acceleration and deceleration and generates large-scale coherent structures. Their characteristics and dynamics depend on the porosity of the obstacle [1]. If the plate porosity is fairly low and the plate is situated very close to the bottom surface, the flow separates and a recirculation region or bubble forms immediately downstream of the plate. Typical examples of such plates used in engineering applications are wind and snow fences and sand barriers positioned close to the ground. The main purpose of snow fences and sand barriers is to trap particles (e.g., snow, sand) on their downstream side by inducing regions of small velocity magnitude that favor particle deposition [2,3].

In most practical applications, the main challenge is to design the porous fence (e.g., snow fence, windbreak barrier, shelter belt) such that it reduces adverse effects induced by snow storms and severe winds [2,4,5]. This reduction can be achieved by a properly designed fence by favoring snow deposition away from the road that it protects [6], by reducing air velocity in the region used as a shelter during hurricanes, or by reducing the wind-blown particle emissions to the environment at industrial sites [2]. In many cases, the width of the fence is much larger than its height, the thickness of the fence is very small compared to its height, and the ground surface is relatively flat. These assumptions simplify the problem, while retaining the main physics. As such, a deep understanding of flow past porous two-dimensional high-aspect-ratio rectangular obstacles is a prerequisite for developing effective designs of porous fences used to control particle drifting, blowing, and deposition in various engineering applications.

Information on the flow structure and on the effect of varying the main geometrical parameters of the porous fence or plate is available mainly from field and wind tunnel investigations [7–12]. Many of these studies focused on determining the effect of the plate or fence porosity on the streamwise drag coefficient and the threshold value of the plate porosity above which the main recirculation bubble is no longer in contact with the plate or fence [7,12–15]. Typically this happens for porosities P close to 30%, where the porosity is defined as the total open area of the fence or plate (e.g., fence holes, spacing between solid elements of a fence or plate) divided by its total frontal area excluding the bottom gap. At very large porosities, no bottom-attached recirculation bubble is generated downstream of the fence.

Previous laboratory and field experiments of these flows provided velocity and turbulence measurements in only a limited number of vertical cross sections. Friction velocity distributions on the bottom surface were seldom measured, and this variable was estimated from velocity measurements away from the surface assuming that the law of the wall accurately describes the velocity distribution near the bottom surface. This is generally not the case in the wake of the plate where flow recirculation, adverse pressure gradients, and highly energetic eddies are present. Additional information on the flow field was obtained from Reynolds-averaged Navier-Stokes (RANS) simulations [4,16–18] and two-dimensional (2D) large-eddy simulation (LES) of laboratory-scale experiments (e.g., [19]). For complex separated flows, the RANS approach is not always very accurate and does not provide information of the dynamics of the coherent structures, which is essential to understand the flow physics [20]. The same is true for 2D LES, which does not account for vortex stretching in the spanwise direction. Recently, Basnet and Constantinescu [21] reported a series of 3D LES of flow past 2D solid and porous plates placed on the channel bottom with no bottom gap. The simulations provided quantitative information on the unsteady forces acting on the plate, the spectral content of the wake, the dynamics of the coherent structures, and the role of the bleeding flow.

A major task when designing porous fences for engineering applications is to determine the optimum bottom gap ratio G/H (G is the distance between the ground surface and the lower edge of the fence) for a given porosity P, such that the particle-retaining capacity of the fence is maximized. For example, without a bottom gap, snow particles will rapidly accumulate close to the downwind face of the snow fence, drastically reducing the capacity of the fence to further retain snow particles in its vicinity. From a fluid mechanics perspective, the presence of a bottom gap induces additional flow complexities and mechanisms for the generation of large-scale coherent structures. As G/H increases, part of the incoming flow is deflected downwards and passes the fence beneath it. As this happens, the flow accelerates and creates a jetlike flow attached to the ground surface, which is the main reason why particles cannot deposit in the immediate vicinity of the fence for sufficiently large bottom gaps. A too large bottom gap will reduce the efficiency of the fence, as the capacity of the fence to induce a region of relatively small velocities close to the ground decreases. Moreover, the general wake structure may also be affected as the separated shear layer (SSL) induced by the flow passing the fence close to its bottom edge starts interacting with the SSL forming at its top edge. As this happens, one expects counter-rotating vortices will be shed in the wake, and the dynamics of these vortices will be similar to that of vortices forming the von Karman vortex street observed past isolated, solid bluff-body obstacles. The presence of a porous obstacle further complicates the problem. Some main results for flow past thin plates and rectangular cylinders with a bottom gap are discussed next.

Durão *et al.* [22] experimentally investigated the mean flow around a square solid cylinder situated in the vicinity of a channel bed for $0 < G/H < 3.3$ at a cylinder Reynolds number, $\mathrm{Re} = 1.36 \times 10^4$. The axis of the cylinder was oriented along the spanwise axis of the channel such that the incoming flow was perpendicular to the upstream face of the cylinder. The onset of large-scale vortex shedding was observed to take place for G/H close to 0.35. The antisymmetric shedding Strouhal number defined with the cylinder height was close to constant ($\mathrm{St} = 0.133$) for

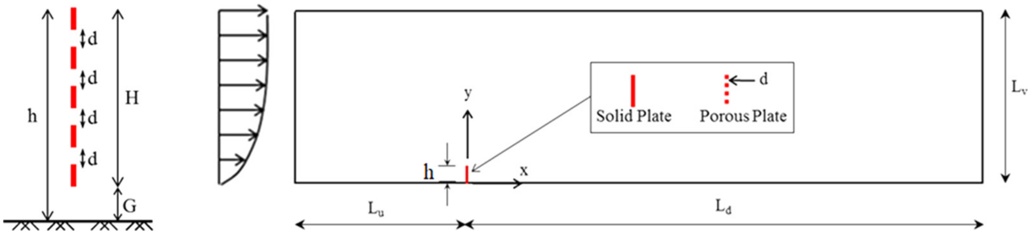

FIG. 1. Sketch showing main variables characterizing a porous plate with a bottom gap (left) and computational domain containing a solid or a porous vertical plate placed in the vicinity of a horizontal surface (right).

$G/H \geqslant 0.35$. Bosch *et al.* [23] investigated the effect of bottom gap on flow past a square cylinder for different values of the bottom gap. In agreement with Durão *et al.* [22], the experimental study of Bosch *et al.* [23] found that the critical value of G/H for suppression or onset of antisymmetric vortex shedding is between $G = 0.35H$ and $G = 0.5H$. In a similar experimental study conducted for $\mathrm{Re} = 18\,900$, Martinuzzi *et al.* [24] found that the bottom SSL reattaches permanently on the channel bed and the large-scale periodic fluctuations are completely suppressed for $G/H < 0.3$. Based on experiments conducted for square cylinders with $0.2 < G/H < 1$ at $\mathrm{Re} = 11\,075$, Panigrahi [25] identified three different types of flow regimes in the wake of the cylinder: (1) complete suppression of vortex shedding at low G/H, (2) transitional regime, where the channel bottom affects the large-scale vortex shedding behind the cylinder ($0.3 < G/H < 0.6$), and (3) (antisymmetric) vortex shedding regime at high G/H, for which the effect of the channel bottom on vortex shedding is negligible.

The case of high-aspect-ratio solid cylinders placed in the vicinity of a channel bed was much less investigated. Cho [26] measured mean flow and turbulence statistics in the wake of a porous thin plate with a bottom gap. Unsteady RANS simulations were reported by Najjar and Vanka [27] for flow past a solid vertical plate placed in uniform flow. An in-depth experimental investigation of the flow past a porous thin fence was performed by Kim and Lee [28] for a fence with $P = 38.5\%$ and $G/H = 0,\ 0.1,\ 0.2$, and 0.3. The plate Reynolds number ($\mathrm{Re_H} = HU_0/\nu$ where U_0 is the incoming velocity and ν is the molecular viscosity) was close to 10^4. Besides providing measurements of the mean velocity and turbulence variables in several vertical sections, they determined the distance from the plate where the SSLs forming at the top and bottom edges start interacting as a function of G/H. Two-dimensional LES was performed by Fang and Wang [29] for flow past porous barriers with $G/H = 0.1$. Two-dimensional LES with a dynamic Smagorinsky model was performed by Huang *et al.* [19] for flow past porous plates with a different porosity over the upper half and lower half of the plate.

In the present study, the physics of turbulent flow past a thin, wide, vertical rectangular plate placed in the vicinity of the ground is investigated as a function of the bottom gap ratio, G/H. The study considers both solid plates and porous plates with a uniform porosity of 36%. The porous plates contain an array of spanwise-oriented (horizontal), identical solid cylinders of rectangular cross section (Fig. 1). The approaching flow is perpendicular to the face of the thin solid cylinders. The height of the solid cylinders and the spacing between them, d, are kept constant. The limiting case in which the plate is in contact with the bottom surface ($G/H = 0$) was already investigated using 3D LES by Basnet and Constantinescu [21].

Two other relevant parameters for flow past porous regions containing cylinders are the ratio between the cylinder diameter d, and a characteristic length scale (e.g., height of the porous plate, H) and the arrangement of the cylinders inside the porous region [30,31]. For example, a regular nonstaggered arrangement of the cylinders inside the porous region induces the formation of high-velocity corridors and is characterized by very different wake-to-cylinder interactions compared to a staggered or random arrangement. This effect is not important for porous regions containing only one vertical array of cylinders (e.g., porous plates). Even if the porosity of the porous region (e.g., porous plate containing rectangular parallel cylinders) is kept constant, the flow paths will be different if a large number of small-diameter cylinders or a smaller number of larger-diameter cylinders is used. So, d/H may be a relevant parameter for flow past porous plates. Basnet and Constantinescu [21] have investigated the effect of varying d/H while maintaining the plate porosity constant for plates in contact with the bottom surface. Though some differences were observed in the instantaneous and main flow fields, varying d/H for constant porosity had a fairly small effect on the main flow features away from the plate and on the main variables of engineering interest (e.g., mean force acting on the plate). Though in the present study the ratio d/H was kept constant, it will be of interest to investigate the effect of d/H for porous plates with a bottom gap and also the effect of using other types of porous plates (e.g., plates containing circular holes that are used for temporary plastic snow fences).

The numerical method, boundary conditions, and code validation are discussed in Sec. II. Section III discusses the main flow and geometrical parameters of the simulations and provides information on the computational domain and computational meshes used to perform the simulations. Section IV investigates the effects of varying the gap aspect ratio, G/H, on the mean flow and turbulence structure around the solid plate, unsteady forces action on the plate, and bed friction velocity distributions on the bottom channel surface. Section V discusses a similar investigation performed for porous plates with $P = 36\%$. Section VI summarizes the main results and provides some concluding comments.

II. NUMERICAL MODEL, BOUNDARY CONDITIONS, AND CODE VALIDATION

The numerical method used to conduct the simulations and the boundary conditions are the same as those used to perform simulations reported in the related study of Basnet and Constantinescu [21]. The finite-volume code [32] solves the conservative form of the incompressible Navier-Stokes equations on nonuniform, Cartesian meshes and discretely conserves the kinetic energy in the computational domain [33]. Periodic boundary conditions are applied in the spanwise (z) direction, as the mean flow is assumed to be two dimensional. The fractional step algorithm uses a staggered, conservative space-time discretization with a semi-implicit iterative method to advance the equations in time. A Poisson equation is solved for the pressure. Central schemes are used to discretise the spatial derivatives in the Navier-Stokes equations. Time discretization is achieved using a Crank-Nicholson scheme for the convective and viscous operators in the momentum (predictor step) equations. The successive over-relaxation (SOR) method is used to solve the system of equations after the governing equations are discretised in both space and time. A blanking technique is used to account for the presence of solid obstacles inside the computational domain. The dynamic Smagorinsky model is used to estimate the subgrid-scale viscosity. The code is parallelized using message passing interface (MPI).

The instantaneous velocity fields at the inflow section of the computational domain (see Fig. 1) are obtained from a preliminary channel flow simulation (no plate) with periodic boundary conditions in the streamwise direction. The velocity is set equal to zero on the channel bottom and on the surfaces of the plate. A symmetry boundary condition is used at the top boundary and a convective boundary condition is used at the outflow boundary [20]. The code was already validated for a wide range of flows including channel flow and flow past obstacles (e.g., isolated circular or rectangular cylinder, arrays of square solid cylinders or dunes mounted at the channel bottom, circular array of solid cylinders) in a straight channel (e.g., see [34–41]).

Of direct relevance for the present study in which antisymmetric wake vortex shedding is expected to occur for cases with a large G/H is the capacity of the code to accurately predict mean velocity and turbulence statistics in the wake of 2D bluff bodies placed at relatively large distances from the domain boundaries. A 3D LES of flow past a wide square cylinder was conducted with the present code. The computational results are compared in Fig. 2 with the experimental results of Lyn *et al.* [42] obtained at a cylinder Reynolds number defined with the length of the cylinder's edge,

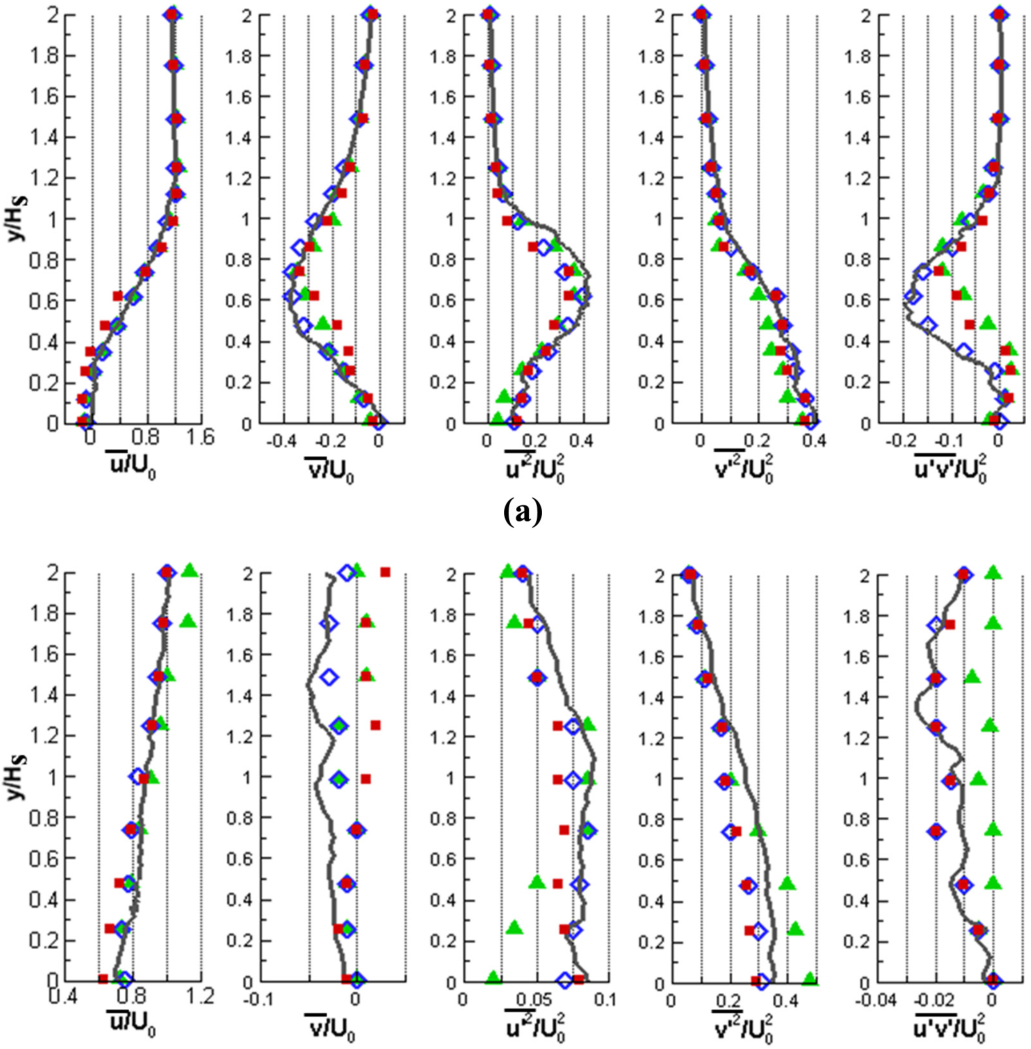

(a)

(b)

FIG. 2. Comparison of streamwise velocity, vertical velocity, streamwise normal Reynolds stress, vertical normal Reynolds stress, and primary shear Reynolds stress profiles for flow past a square solid cylinder at $\mathrm{Re} = U_0 H_s/\nu = 21\,400$. 3D LES results, present study: solid line; experimental results of Lyn *et al.* [42]: red squares; LES results of Wang and Vanka [43]: green triangles; and LES results of Srinivas *et al.* [44]: blue circles. (a) $x = 1H_s$; (b) $x = 5H_s$ where the center of the square cylinder is situated at $x = 0$ and its edge length is H_s.

H_s, of 21 400. The streamwise length of the computational domain in the present LES was $35H_s$, its width was $3.5H_s$, and its height was $14H_s$. The cylinder was placed at equal distances from the top and bottom extremities of the channel, the same as in the corresponding experiment. Also included in Fig. 2 are LES results reported by Wang and Vanka [43] and by Srinivas *et al.* [44]. The blockage ratio was 0.07 in the present LES, which is close to the values in the other simulations reported for this case. The flow was steady and uniform in the inflow section and a convective boundary condition was used at the outflow boundary.

The mean velocity profiles together with those of the normal and main shear Reynolds stresses are compared in Fig. 2 at two streamwise locations, $x = 1H_s$ and $x = 5H_s$, where $x = 0H_s$ corresponds to the center of the square cylinder. Only half of the domain is shown ($y > 0$), as the mean flow is symmetrical with respect to the center line of the cylinder ($y = 0H_s$). The profile at $x = 1H_s$ cuts through the mean flow separation bubble at the back of the cylinder. The level of agreement between the present LES and experiment is good for the mean velocity components (error with respect to the experiment is less than $0.05U_0$ at most locations). Present LES results are, in general, very close (e.g., within $0.02U_0$) to those of Wang and Vanka [43]. The peak streamwise normal stresses occur in the SSLs forming on the sides of the square cylinder. As one moves away from the back of the cylinder, the peak moves closer to the center line. Larger differences between the present LES and experiment are observed for the primary mean shear stress at $x = 1H_s$ where present LES predictions are very close to those of Wang and Vanka [43]. Meanwhile, the predictions of Srinivas *et al.* [44] are closer to the experimental measurements. However, the opposite is true at $x = 5H_s$ where the profiles of the Reynolds stresses predicted by the present LES and Wang and Vanka [43] are closer to the experimental measurements compared to Srinivas *et al.* [44]. The mean value of the drag coefficient corresponding to the streamwise force acting on the square cylinder predicted by the present 3D LES is 2.11. Lyn *et al.* [42] obtained a value of 2.1 based on their measurements, while the other 3D LES predicted 2.03 and 2.14. The Strouhal number ($\mathrm{St}' = f'H_s/U_0$, where f' is the frequency) corresponding to the antisymmetric shedding frequency was 0.132, which is very close to the experimentally determined value (0.132) and the values predicted by the other two LES (0.13 and 0.135). No experimental values were reported for the root-mean-square (rms) fluctuations of the streamwise drag and vertical drag (lift) coefficients, but the values predicted by the present LES (0.21 and 1.50) are close to those predicted by the other two LES. Basnet and Constantinescu [21] report validation results for the flow past a 2D solid thin plate placed perpendicular to the incoming flow in a wide channel at a plate Reynolds number of 21 400. The predictions of the mean streamwise drag coefficient and the rms fluctuations of the streamwise and vertical drag coefficients were also found to be very close to the experimentally determined values.

III. SIMULATIONS SETUP AND PARAMETERS OF THE TEST CASES

In a streamwise-vertical (x-y) plane, the origin of the system of coordinates is situated on the channel bottom at the intersection with the vertical line cutting through the middle of the plate (Fig. 1). The plate of height H and thickness $t = 0.02H$ is placed at a distance G from the channel bottom. The plate is located at a distance $L_u = 10H$ from the inflow section and at a distance $L_d = 25H$ from the outflow section. The domain height is $L_v = 10H$ and the domain width is $L_z = 3H$. All simulations were conducted with $\mathrm{Re_H} = \mathrm{HU_0}/\nu = 20\,000$ where U_0 is the mean (section-averaged) incoming velocity in the channel. These simulations mimic experiments conducted at a laboratory scale (e.g., for $H = 0.1$ m and $U_0 = 2$ m/s, which is typical of small wind tunnels where such experiments are conducted). At field scale, the Reynolds numbers are about two orders of magnitude higher [6]. The solid elements of the porous fence are disposed along the spanwise direction and have a rectangular shape ($0.06H$ height and $0.02H$ width). The distance between the solid elements is $d = 0.04H$.

Two series of five simulations were conducted. A first series of simulations was performed for solid plates ($P = 0\%$) for $G = 0H, 0.1H, 0.2H, 0.5H$, and H to investigate the effect of the bottom gap ratio, G/H, on the flow structure. Then, a similar series of five simulations was performed for porous plates with $P = 36\%$.

The computational domain was meshed with close to 19 million grid points. The mesh spacing was uniform in the spanwise direction. The mesh point distributions along the x and z directions were such that the viscous sublayer on all solid surfaces, including the surfaces of the solid elements of the porous plate, were resolved. The wall-normal nondimensional distance corresponding to the first mesh point off each solid surface was less than 2 wall units at all locations. Away from the

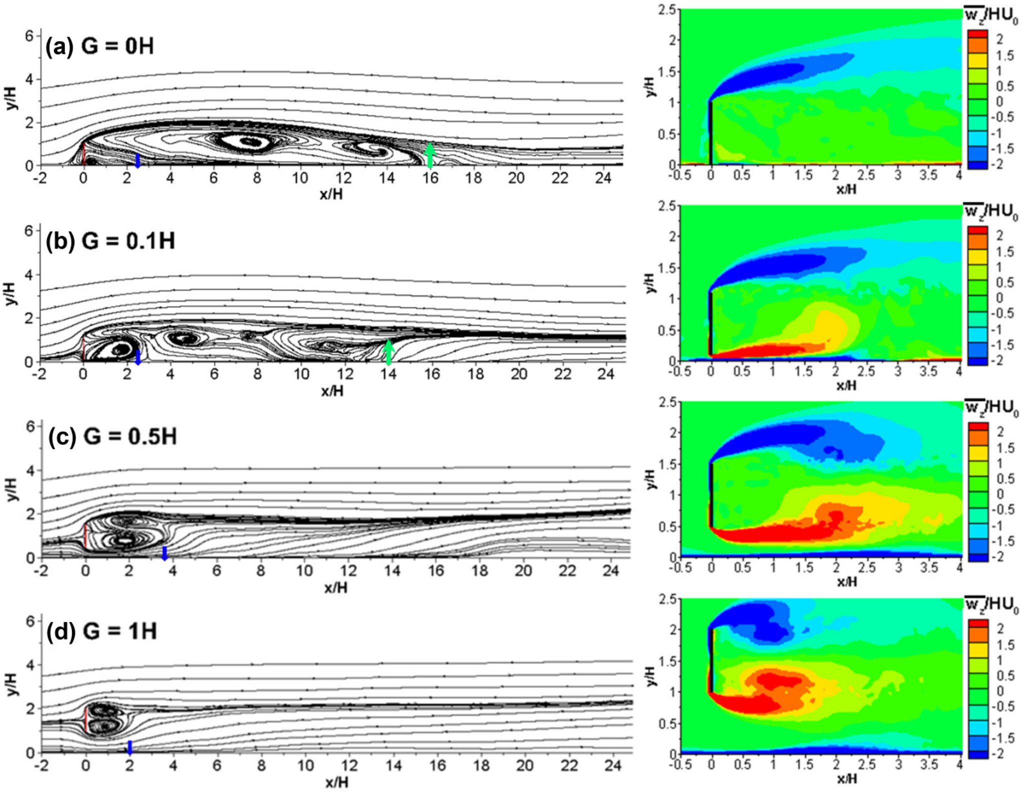

FIG. 3. Mean flow structure visualized using 2D streamline patterns for the solid plate ($P = 0\%$) cases. The blue and green lines indicate the end of the separation bubble at the back of the solid plate and the end of the main bottom-attached recirculation bubble for cases with low G/H, respectively. Also shown are the mean spanwise vorticity, $\bar{\omega}_z/(H/U_0)$, distributions.

plate, the average dimensions of the 3D cells were close to $0.06H$. This resolution corresponds to close to 100 wall units. The time step was $\Delta t = 0.001H/U_0$. Though the instantaneous eddy viscosity values predicted by the dynamic Smagorinsky model in the regions containing turbulent eddies and/or high shear were relatively low (e.g., of the order of the molecular viscosity, which is also an indication of a well-resolved LES), the dissipation provided by the subgrid-scale model was critical to obtain a converged solution.

IV. EFFECT OF BOTTOM GAP RATIO FOR SOLID PLATES

A. Mean flow and turbulent kinetic energy

In the case where the plate is in contact with the channel bottom ($G = 0H$), there is only one SSL forming at the top edge of the plate. For the other cases, a second SSL forms at the bottom edge of the plate. They will be referred to as the top SSL and the bottom SSL, respectively. As shown by the 2D streamline patterns in Fig. 3, a recirculation bubble forms in between the plate and the channel bottom for $G/H \leqslant 0.2$ and a separation bubble forms behind the plate for $G/H \geqslant 0.5$. The length of the main recirculation bubble, l_1, decreases monotonically with the increase in G/H (see Table I), while its maximum height, h_1, remains close to constant ($1.8H$). Even in the $P = 0\%$ $G = 0.2H$ case where the antisymmetric shedding is not present, a separation bubble containing two eddies forms behind the plate and is contained within the recirculation bubble. The length of the separation bubble, l_2, decreases monotonically with the increasing G/H (Table I). In the $P = 0\%$

TABLE I. Effect of bottom gap ratio, G/H, on the variables characterizing the streamwise force acting on the solid plate ($P = 0\%$), the size of the separation bubble forming behind the plate or of the recirculation bubble attached to the channel bed, and the nondimensional frequency of the passage of billow vortices associated with the antisymmetric wake shedding, $\mathrm{St_w}$.

Case	$\bar{C}_\mathrm{D}$	C_D^{rms}	l_1	h_1	l_2	$\mathrm{St_w}$
$P = 0\%, G = 0H$	0.78	0.03	$16.2H$	$1.8H$		
$P = 0\%, G = 0.1H$	0.89	0.04	$14.0H$	$1.8H$		
$P = 0\%, G = 0.2H$	0.93	0.045	$12.5H$	$1.8H$	$4.2H$	
$P = 0\%, G = 0.5H$	1.11	0.06			$3.8H$	0.12
$P = 0\%, G = H$	1.57	0.2			$2.0H$	0.14

$G = 1H$ case, its length is very close to that predicted for $G/H \gg 1$. For $G/H = 0.5$, the size of the bottom eddy inside the separation bubble is larger. For $G = 1H$, the sizes of the two eddies are approximatively equal.

The spanwise vorticity distributions in Fig. 3 show that the largest amplification of the vorticity in the mean flow occurs over the upstream part of the SSLs. The penetration length of the region of high spanwise vorticity magnitude associated with the top SSL increases monotonically with G/H until $G/H = 0.2$ and then starts decreasing with increasing G/H. A similar behavior is observed for the bottom SSL whose strength (e.g., as characterized by the vorticity magnitude levels inside it and its length) peaks around $G/H = 0.5$. Due to the larger flow acceleration occurring in the gap region, the lower SSL is stronger than the top SSL for $G/H \geqslant 0.5$.

The distributions of the turbulent kinetic energy (TKE) in Fig. 4 show a significant amplification of the turbulence inside the region where billows are shed from the top and bottom SSLs. Once the antisymmetric vortex shedding occurs, the highest TKE values are predicted in the region where the wake billows form. A strong decay of the TKE is observed on the bottom side of the wake downstream of the location where the billows originating in the bottom SSL lose their coherence (e.g., at $x = 6H$ for $G = 0.5H$ and at $x = 8H$ for $G = 1H$; see Fig. 4). Downstream of this location, the TKE increases with increasing G/H (see TKE profiles at $x/H = 8$ in Fig. 4).

B. Instantaneous flow fields

Among the five cases, the $P = 0\%$ $G = 0H$ case is the one where the mean shear across the top SSL is the highest because all the incoming flow is diverted upwards and then past the top edge of the plate. This induces a strong flow acceleration on the outer-flow side of the top SSL. As a result, the production of turbulence inside the top SSL is the largest and the SSL vortex tubes are more coherent compared to $G/H > 0$ cases (see ω_z distributions in Fig. 5). Merging of vortex tubes results in the formation of larger vortical eddies and the thickening of the top SSL. At the end of the main recirculation bubble forming immediately behind the plate, these large vortical eddies start interacting with the channel bed. At times, part of the core of these eddies is injected into the recirculation bubble at the back of the plate. These vortical eddies are then advected toward the plate and then toward the upstream part of the top SSL, where they strongly disturb the eddies advected inside the SSL. This creates a feedback mechanism that induces strong disturbances and stretching of the vortex tubes shed over the upstream part of the top SSL.

As G/H increases, the mean vorticity magnitude inside the bottom SSL increases monotonically. Even for relatively small values of the gap aspect ratio ($G/H = 0.1$), the bottom SSL curves toward the top SSL. At times when the end of the bottom SSL approaches the top SSL [see ω_z distribution in Fig. 5(b) where the bottom SSL interacts with the top SSL around $x = 2H$], the evolution of the corotating eddies advected in the top SSL is affected. This favors the merging of several of these corotating eddies into a larger eddy that resembles a wake billow generated for flows where the

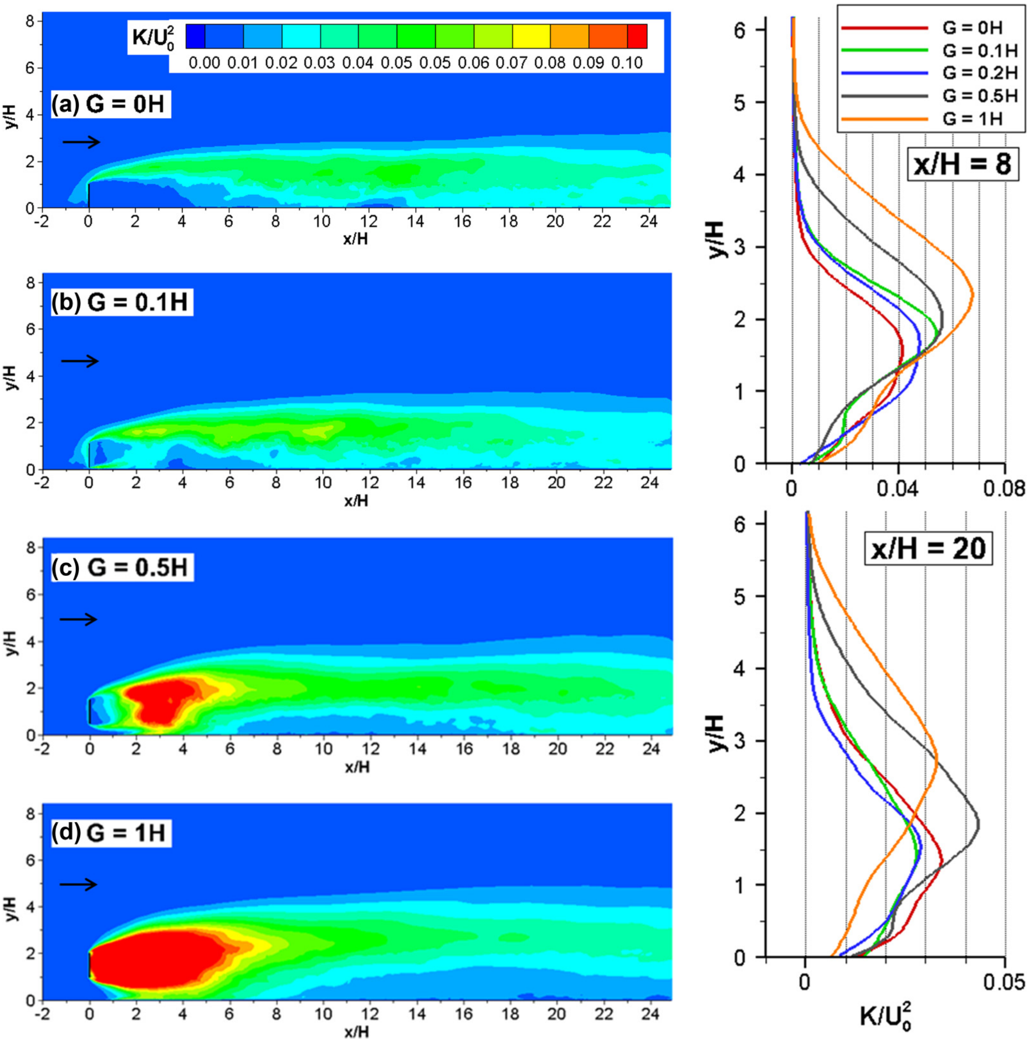

FIG. 4. Turbulent kinetic energy, K/U_0^2, in an x-y plane for the solid plate ($P = 0\%$) cases. Also shown are vertical profiles of K/U_0^2 at $x/H = 8$ and $x/H = 20$.

antisymmetrical vortex shedding is observed. The top SSL in the $P = 0\%$ $G = 0.1H$ case contains several of these large billows. The coherence of the billows forming in the top SSL increases with G/H as stronger interactions are observed between the bottom and the top SSLs. For $G/H \geqslant 0.5$, the top SSL curves sufficiently toward the bottom SSL such that counter-rotating wake billows form quasiregularly and the antisymmetric vortex shedding mode is observed. For $G/H = 0.5$, the wake billows form at a larger distance from the plate compared to the case ($G/H \gg 1$) where the channel bottom has a negligible effect on the flow.

For $G/H = 1$, the acceleration of the flow through the bottom gap is not significantly larger than that of the flow around the top edge of the plate and the billows originating from the bottom and top SSLs form fairly close behind the plate, similar to what is observed for $G/H \gg 1$. Though very close to the plate, the flow in the $P = 0\%$ $G = 1H$ case resembles the one for plates with $G/H \gg 1$; this is not the case at larger distances [e.g., for $x/H > 2$ in Fig. 5(d) showing ω_z] where the billows shed from the bottom SSL start interacting with the channel bottom. As a billow approaches the

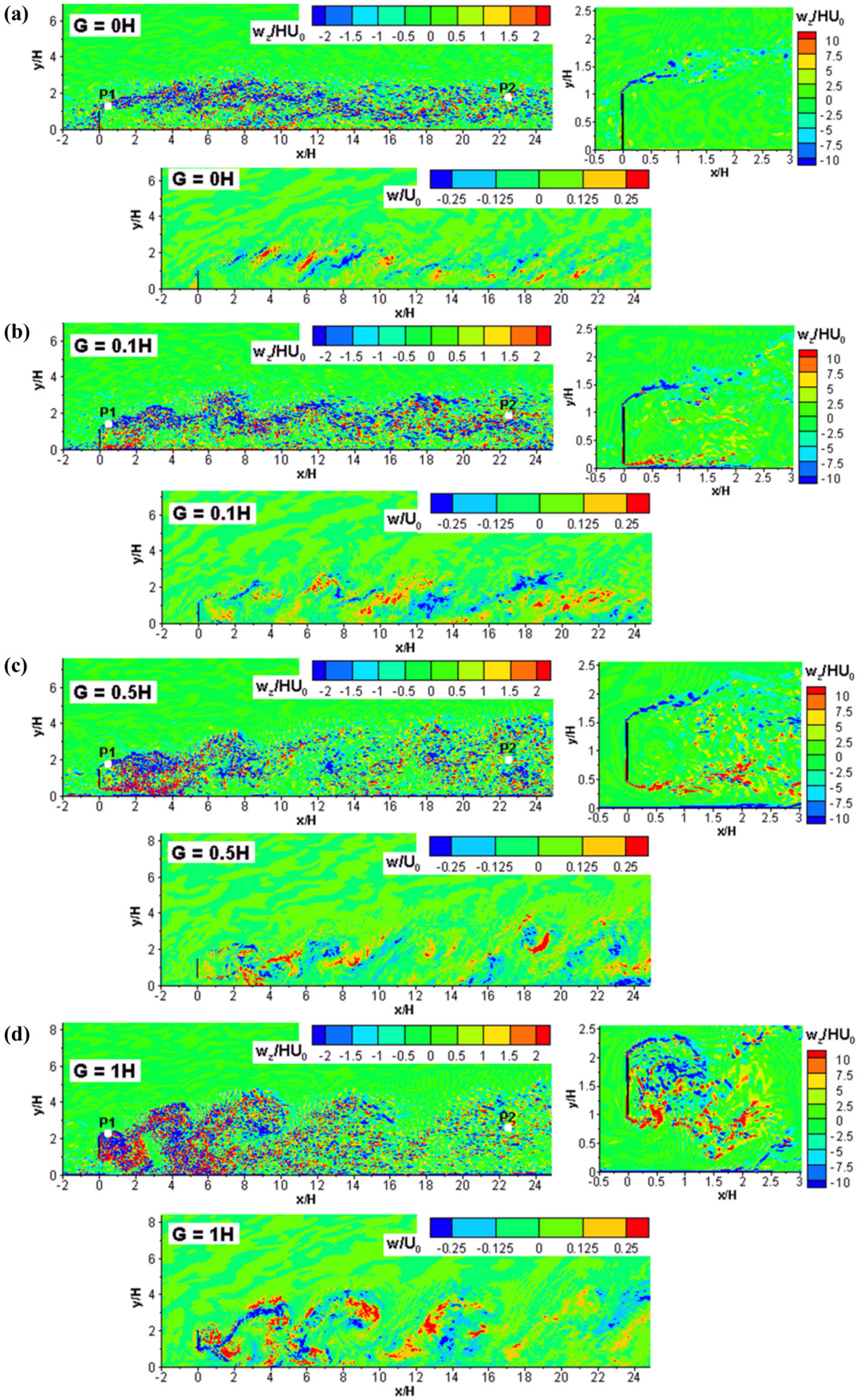

FIG. 5. Instantaneous spanwise vorticity, $\omega_z/(H/U_0)$, and spanwise velocity, w/U_0, in an x-y plane for the solid plate ($P = 0\%$) cases. (a) $G = 0H$; (b) $G = 0.1H$; (c) $G = 0.5H$; (d) $G = 1.0H$.

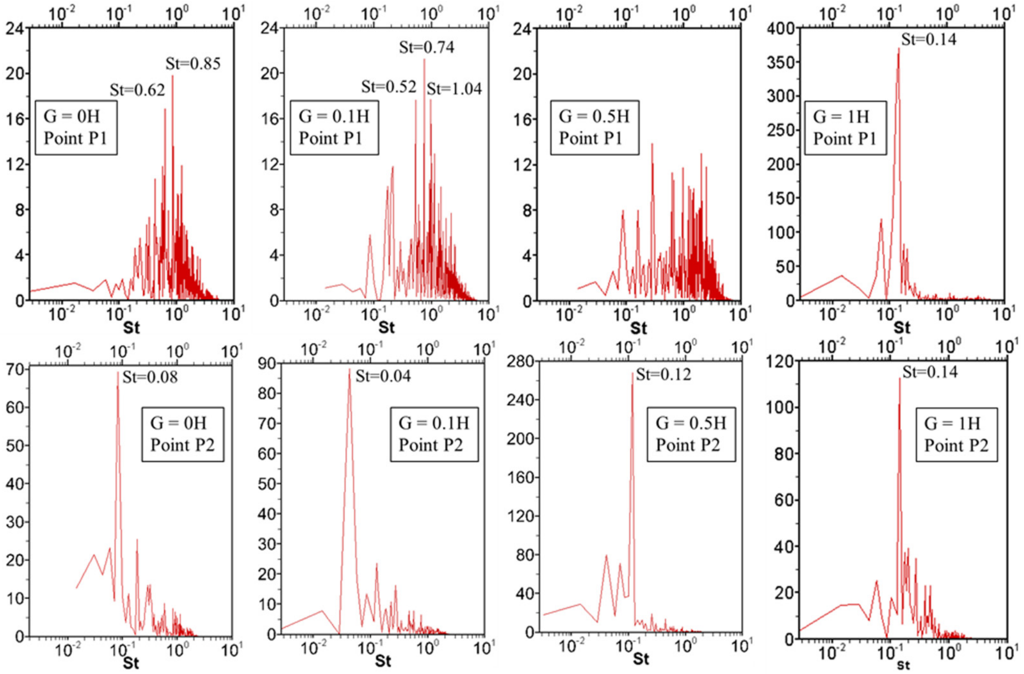

FIG. 6. Power spectra of the vertical velocity at point P1 and point P2 for the solid plate ($P = 0\%$) cases. The positions of points P1 and P2 are shown in Fig. 5. The power spectra are compared for the $G = 0H$, $G = 0.1H$, $G = 0.5H$, and $G = 1.0H$ cases.

channel bottom [e.g., this happens around $x/H = 4$ in Fig. 5(d)], it slows down and its capacity to rotate around its axis is reduced. The billow starts losing its coherence via vortex stretching. For the $P = 0\%$ $G = 1H$ case, the passage of two successive billows from the top SSL is enough to destroy most of the coherence of a bottom SSL billow trapped in the bottom boundary layer. This is why for $x/H > 8$, the wake flow in the $P = 0\%$ $G = 1H$ case contains only large billows originating in the top SSL. For cases where billows originating in the bottom SSL form ($G/H \geqslant 0.5$), the coherence of the billows originating in the top SSL is significantly larger with respect to cases with a relatively small G/H ($\leqslant$0.2).

Given that the mean flow is 2D, the distributions of the instantaneous spanwise velocity in Fig. 5 give an indication on the degree of flow three dimensionality inside the SSLs and the wake. Elongated patches of high positive and negative spanwise velocity are observed in all $P = 0\%$ cases inside the wake region. The velocity magnitude inside these patches is of the order of $0.3U_0$, which means that the spanwise transfer of momentum is significant. By comparison, the spanwise velocity magnitude in the incoming fully developed, free stream flow (no obstacle) is about six times lower. In the simulations with $G/H < 0.5$, a patch of positive spanwise velocity is situated in the immediate vicinity of a patch of negative spanwise velocity, at most locations. Most of these patches are situated in the region where the billow from the top SSL are advected. Only in the $P = 0\%$ $G = 1.0H$ case, strong patches of high and low spanwise velocity are also observed in the bottom SSL. The formation of coherent billows originating in either the top or bottom SSLs is the main mechanism responsible for the amplification of momentum transport in the spanwise direction.

In the $P = 0\%$ $G = 0H$ case, the two most energetic frequencies in the top SSL, close to its origin, correspond to a Strouhal number, $\mathrm{St} = fH/U_0$ (f is the frequency), of 0.62 and 0.85, respectively (see velocity power spectrum at point P1 in Fig. 6). These two frequencies are induced by the most energetic SSL vortex tubes. In the $P = 0\%$ $G = 1H$ case, the velocity spectrum at point P1 contains one dominant frequency, $\mathrm{St} = 0.14$, which is the shedding frequency of the counter-rotating billows and is denoted $\mathrm{St_w}$ in Table I. This frequency is so energetic close to the origin of the top SSL because the wake billows are forming very close to the plate in the $P = 0\%$ $G = 1H$ simulation, which is not the case in the $P = 0\%$ $G = 0.5H$ simulation where the antisymmetric wake mode is also observed.

In the $P = 0\%$ $G = 0H$ case, the largest vortical eddies in the top SSL continue to grow and eventually start interacting with the bed as the mean flow reattaches around $x = 16H$. Downstream of this location, the dominant frequency in the velocity spectra associated with the passage of the largest eddies generated in the top SSL is $\mathrm{St} = 0.08$ (see spectrum at point P2 for $G = 0H$ in Fig. 6). Vortex merging between successively shed eddies is the main mechanism responsible for the growth of these eddies until around $x = 12H$, downstream of which no vortex merging events are observed. In the $P = 0\%$ $G = 0.1$ case, the dominant frequency in the velocity spectra is $\mathrm{St} = 0.04$ at locations situated downstream of the main recirculation bubble (e.g., see spectrum at point P2 in Fig. 6). The bottom SSL interacts with eddies shed in the top SSL. These interactions occur at around $x = 2.0H$ and the dominant frequency associated with these interactions is close to $\mathrm{St} = 0.08$. In between $x \approx 2.0H$ and $x \approx 14H$, where the mean flow reattaches, one merging event occurs within the top SSL, such that the dominant frequency associated with the passage of the large billows advected parallel to the channel bottom (e.g., at point P2; see Fig. 6) is $\mathrm{St} = 0.04$.

For $G/H \geqslant 0.5$, the mechanism responsible for the formation of large billows inside the top and bottom SSLs is basically the same as that observed for plates with $G/H \gg 1$ for which counter-rotating wake billows of comparable circulation are shed with a frequency close to $\mathrm{St_w} = 0.14$–0.15 [21,45]. For the $P = 0\%$ $G = 0.5H$ and $P = 0\%$ $G = 1H$ cases, the billows shed from the bottom SSL are of comparable circulation to that of the billows shed from the top SSL in the formation region. Their shedding frequency is $\mathrm{St_w} = 0.12$ in the $G = 0.5H$ case and $\mathrm{St_w} = 0.14$ in the $G = 1H$ case (see main peaks in the corresponding power spectra at point P2 in Fig. 6). The main difference between the $G = 0.5H$ and $G = 1H$ simulations and the limiting case with $G/H \gg 1$ ratio is that the billows shed from the bottom SSL start interacting with the channel bottom [Figs. 5(c) and 5(d)]. As this happens, their advection velocity and circulation decays. Severe vortex stretching occurs as the billows that are shed from the top SSL approach the slowly moving billow trapped into the boundary layer on the channel bottom.

C. Forces acting on the plate

Figure 7 shows the effect of varying G/H on the net width-averaged mean nondimensional pressure distribution over the plate. The presence of the bottom gap results in decreasing the pressure difference between the front and back faces of the plate close to its bottom edge. Away from the two edges, the pressure distribution on the plate is fairly symmetrical with respect to the middle of the plate for $G/H > 0$.

Table I and Fig. 8 show the effect of increasing G/H on the mean streamwise drag coefficient acting on the plate,$\bar{C}_\mathrm{D}$, and its rms fluctuations, C_D^{rms}, for the $P = 0\%$ cases. The mean drag coefficient increases monotonically with increasing G/H toward the value ($\bar{C}_\mathrm{D} = 2.13$–$2.17$) expected for $G/H \gg 1$ [21,46]. Still, the effect of the bottom wall on $\bar{C}_\mathrm{D}$ is not negligible even for the $P = 0\%$ $G = 1H$ case as its value (1.57) is still significantly smaller than the one predicted for $G/H \gg 1$. This is not surprising given that significant interactions take place between billows forming from eddies shed in the bottom SSL and the channel bottom for $G/H = 1$. The rms of the drag coefficient fluctuations, C_D^{rms}, increases monotonically with increasing G/H. Once the antisymmetric vortex shedding occurs ($G/H \geqslant 0.5$), the rate of increase of C_D^{rms} is larger. In the $P = 0\%$ $G = 1H$ case, the billows form immediately behind the plate, as also observed for

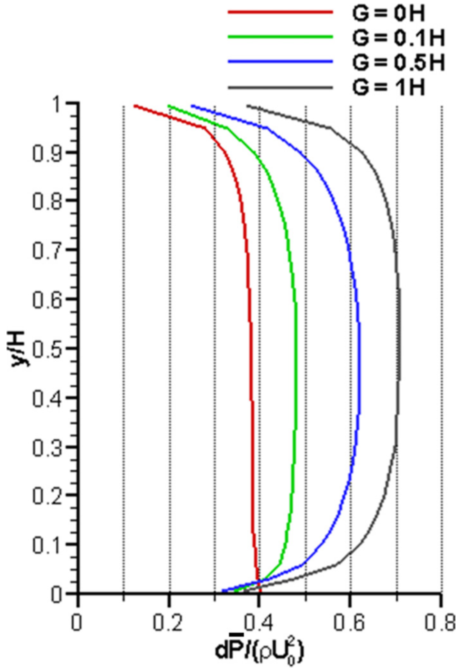

FIG. 7. Spanwise- and time-averaged net pressure distribution on the plate for the solid plate ($P = 0\%$) cases, where y/H represents the vertical distance from the bottom edge of the plate.

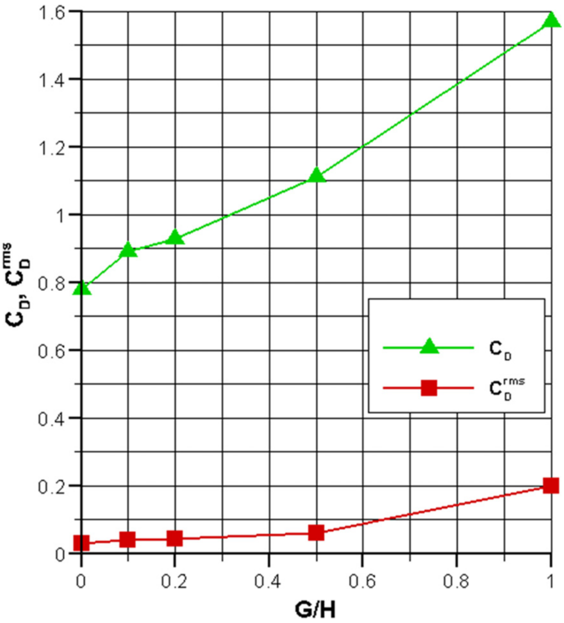

FIG. 8. Effect of varying the bottom gap, G/H, on the mean drag coefficient and the rms fluctuations of the drag coefficient for the solid plate ($P = 0\%$) cases.

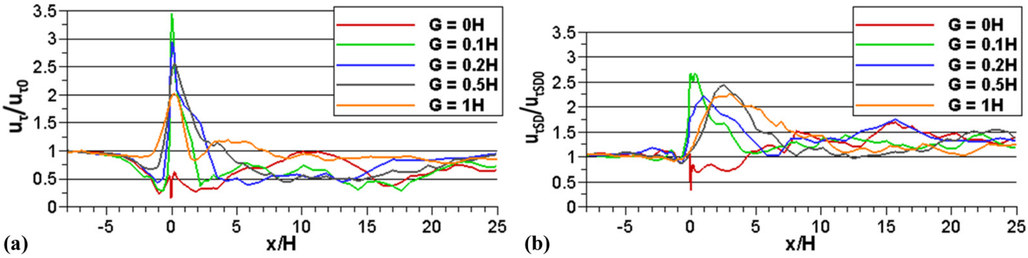

FIG. 9. Effect of G/H on the (a) nondimensional, spanwise-averaged bed friction velocity magnitude in the mean flow and (b) nondimensional rms fluctuations of the bed friction velocity, $u_{\tau\mathrm{SD}}$ for the solid plate ($P = 0\%$) cases.

$G/H \gg 1$. This is why the predicted value of C_D^{rms} $(= 0.2)$ for $G/H = 1$ is quite close to the value (0.24) expected for $G/H \gg 1$ [21].

D. Bed friction velocity

The spanwise-averaged distributions of the nondimensional mean bed friction velocity magnitude in Fig. 9(a) allow estimating the spatial extent of the region where the bed friction velocity, u_τ, is amplified with respect to the mean value in the incoming fully developed flow, $u_{\tau 0}$, which is close to $0.04U_0$. The flow advected through the bottom gap leads to a significant amplification of $u_\tau/u_{\tau 0}$ over some distance from the plate. For $G/H \geqslant 0.1$, the peak value within this region decreases monotonically with increasing G/H (e.g., from about 3.5 for $G = 0.1H$ to about 2.0 for $G = 1H$). The length of the region where $u_t/u_{t0} \geqslant 1$ is the largest for $G/H \approx 0.2$. For the $P = 0\%$ $G/H = 1$ case, a second region of amplification of u_τ is observed around the location where the billows shed from the bottom SSL reach the channel bottom. As expected, $u_\tau/u_{\tau 0} < 1$ in the wake of the plate for the $P = 0\%$ $G = 0H$ case where a large bottom-attached recirculation bubble forms.

Besides inducing regions of large u_τ, the interaction of the incoming flow with the plate also induces regions of large rms bed friction velocity fluctuations, $u_{\tau\mathrm{SD}}$. These latter regions are situated where energetic coherent structures are advected in the vicinity of the channel bottom. The passage of such coherent structures (e.g., billows originating in the bottom SSL for $G/H \geqslant 0.5$) can substantially amplify the capacity of the flow to entrain particles in the case of a loose channel bed compared to that estimated based only on the mean u_τ. The length of the region situated downstream of the plate where $u_{\tau\mathrm{SD}}$ is larger than the value associated with the fully developed incoming turbulent flow ($u_{\tau\mathrm{SD}0} = 0.0025\,U_0$) increases from $4.5H$ for $G/H = 0.1H$ to $15H$ for $G/H = 1$.

Figure 10 shows the distributions of the streamwise velocity in a plane parallel to the channel surface situated at a distance of $0.0055H$ from the channel bottom. The magnitude of u_τ is strongly correlated with the distribution of the near-bed streamwise velocity. As expected, streaks of high and low near-bed streamwise velocity form upstream of the plate. For the low G/H cases, where a recirculation eddy forms starting at the back of the plate, no streaks are observed inside and immediately downstream of the main recirculation bubble. Rather, patches of large negative streamwise velocity are present over the downstream half of the main recirculation bubble close to the bed. They are induced by the energetic eddies forming as a result of the interaction of the large billows in the top SSL with the channel bottom. Part of these billows is reinjected into the main recirculation bubble. For $G/H > 0.2$, the streaks become stronger in the flow acceleration region starting at the plate location (e.g., $0H < x < 2H$ for $G/H = 1$ in Fig. 10). Then irregular patches of high positive near-bed streamwise velocity are observed at locations where billows from the bottom SSL hit the channel bottom (e.g., around $x = 6H$ for $G/H = 1$).

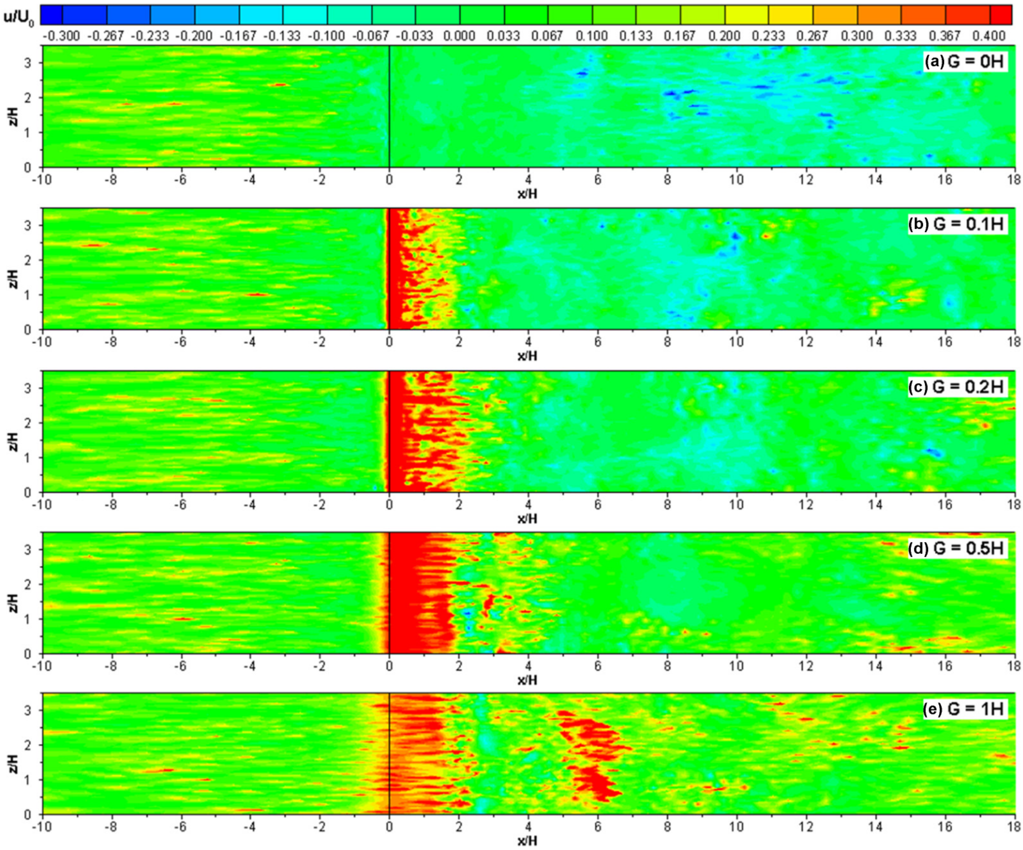

FIG. 10. Instantaneous streamwise velocity, u/U_0, distribution on a horizontal plane situated at a distance of $0.0055H$ from the bottom surface for the solid plate ($P = 0\%$) cases. (a) $G = 0H$; (b) $G = 0.1H$; (c) $G = 0.2H$; (d) $G = 0.5H$; (e) $G = 1.0H$.

V. EFFECT OF BOTTOM GAP RATIO FOR POROUS PLATES

A. Mean flow and turbulent kinetic energy

As opposed to the $P = 0\%$ $G = 0H$ case, where a large recirculation bubble forms behind the plate [Fig. 3(a)], the main recirculation bubble in the $P = 36\%$ $G/H = 0$ case forms far from the plate [Fig 11(a)]. It extends from $x = 8.5H$ to $x = 13H$ and its maximum height is $0.5H$ (Table II). For $G/H > 0$, a recirculation bubble does not form at the channel bottom.

A second plate-attached recirculation bubble forms at a lower height, where the bleeding flow through the fence divides into a component that is advected toward the top SSL and a component that is advected toward the bottom SSL (Fig. 11). For $G/H \leqslant 1$, the point on the plate where the flow splits is situated slightly beneath the middle height of the plate. For $0.1 \leqslant G/H \leqslant 1$, the percentage of the discharge advected toward the lower SSL with respect to the total bleeding flow discharge is fairly constant ($\approx 31\%$). For $G/H \gg 1$, the ratio of the two components is expected to approach one and the recirculation bubble to be symmetrically positioned with respect to the middle height of the plate. The size of this bubble increases monotonically with G/H.

The distributions of the spanwise vorticity in the mean flow (Fig. 11) show that the top SSL is stronger (e.g., in terms of the size of the high vorticity magnitude region) than the bottom SSL until $G/H \approx 0.3$. This is because, for very small G/H values, only a small part of the incoming flow approaching the upstream side of the porous plate is diverted through the bottom gap. As G/H

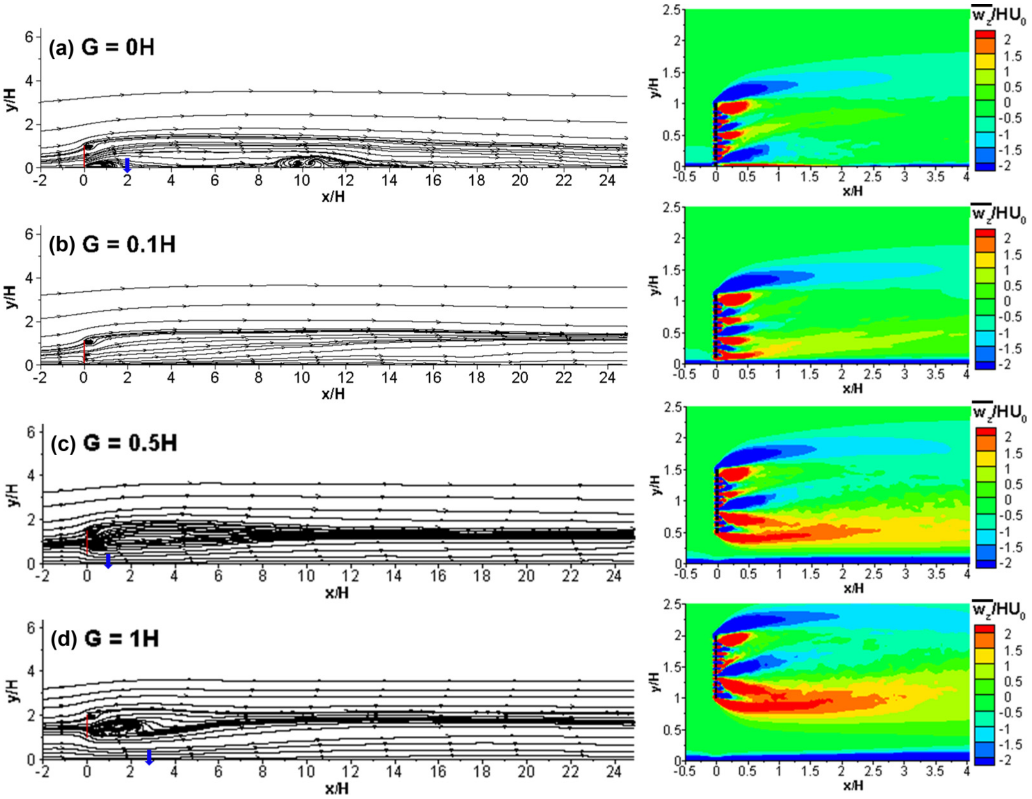

FIG. 11. Mean flow structure visualized using 2D streamline patterns for the porous plate ($P = 36\%$) cases. The blue lines indicate the end of the separation bubble at the back of the solid plate. Also shown are the mean spanwise vorticity, $\bar{\omega}_z/(H/U_0)$ distributions.

increases, a larger percentage of this part of the incoming flow is diverted into the bottom gap. Moreover, the channel bottom limits the opening through which this flow can pass the plate, which results in a further acceleration of the flow through the gap opening. The maximum difference in the strengths of the two SSLs is observed for $G/H = 0.5$ [Fig. 11(c)]. As G/H is further increased, the length of the bottom SSL decreases [Fig. 11(d)]. It is expected that for $G/H \gg 1$, the length and vorticity magnitude levels inside the two SSLs will become equal. For the cases where the

TABLE II. Effect of bottom gap ratio, G/H, on the variables characterizing the streamwise force acting on the porous plate ($P = 36\%$), the size of the separation bubble forming behind the plate or of the recirculation bubble attached to the channel bed, the nondimensional frequency of passage of the billow vortices associated with the antisymmetric wake shedding, $\mathrm{St_w}$, and the volumetric flow rate per unit width of the bleeding flow through the plate, q.

Case	$\bar{C}_\mathrm{D}$	$C_\mathrm{D}^\mathrm{rms}$	l_1	h_1	l_2	$\mathrm{St_w}$	$q/(U_0H)$
$P = 36\%, G = 0H$	0.56	0.06	$4.5H$	$0.5H$			0.085
$P = 36\%, G = 0.1H$	0.62	0.06			$0.25H$		0.089
$P = 36\%, G = 0.2H$	0.65	0.07			$0.45H$		0.090
$P = 36\%, G = 0.5H$	0.78	0.08			$0.95H$	0.13	0.092
$P = 36\%, G = H$	0.88	0.09			$2.3H$	0.16	0.097

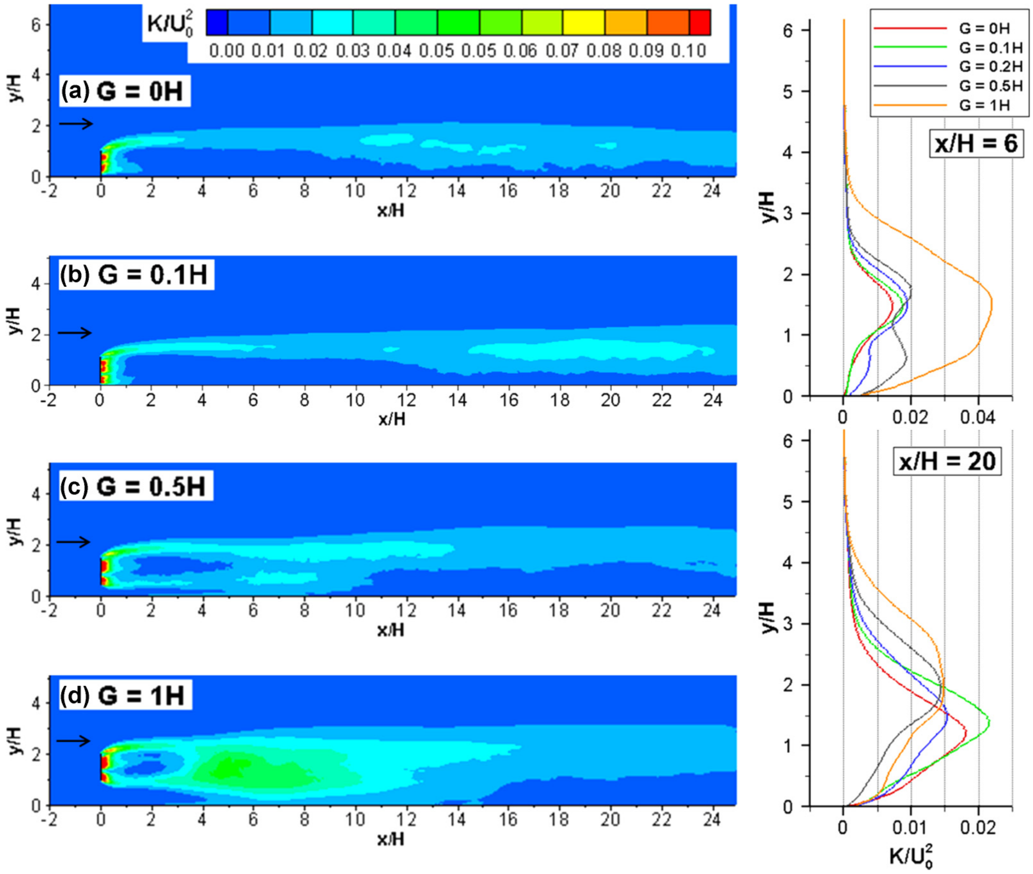

FIG. 12. Turbulent kinetic energy, K/U_0^2, in an x-y plane for the porous plate ($P = 36\%$) cases. Also shown are vertical profiles of K/U_0^2 at $x/H = 6$ and $x/H = 20$.

antisymmetric wake vortex shedding is present, the length of the bottom SSL and the distance at which wake billows are forming increase with increasing plate porosity for constant G/H [Figs. 3(d) and 11(d)].

For the same G/H, the TKE in the SSLs and the wake region are, on average, about two times smaller in the porous plate simulations compared to the solid plate simulations (Figs. 4 and 12). For porous plates with $G/H \geqslant 0.5$, the TKE levels in the bottom SSL are comparable to those observed in the top SSL (Fig. 12). For cases where the antisymmetric wake vortex shedding is observed (e.g., case $P = 36\%$ $G = 1H$), the TKE levels in the region where billows from the top and bottom SSLs interact increase with increasing G/H [Figs. 12(c) and 12(d)]. These results are consistent with those observed for solid plates. In the downstream part of the near wake, the TKE amplification in the top SSL is the largest in the cases where the antisymmetric vortex shedding is not present and peaks for $G/H = 0.1$.

B. Instantaneous flow fields

In the $P = 36\%$ cases, only a fraction of the incoming flow is deflected around the plate; the other part is advected through the plate and forms the bleeding flow. Results in Table II show that the bleeding flow rate increases mildly with increasing G/H for constant porosity (Table II). The mean shear driving the growth of the Kelvin-Helmholtz instabilities in the top SSL is smaller in the porous plate cases compared to the corresponding solid plate cases. This is why, for the same value of G/H, the top SSL is always weaker for a porous plate compared to a solid plate.

The eddy structure of the top SSL in the $P = 36\%$ $G = 0H$ case [see ω_z distributions in Fig. 13(a)] looks qualitatively similar to the one observed for a solid plate [Fig. 5(a)]. The large billows generated in the downstream part of the top SSL interact with the channel bottom past the downstream end of the main recirculation bubble. The bleeding flow is characterized by the presence of highly energetic eddies generated by the jets forming in between the solid elements of the porous plate. The streamwise momentum of the bleeding flow decays with the distance from the plate. Its main role is to impede the rapid reattachment of the top SSL to the channel bottom. Compared to the $P = 0\%$ $G = 0H$ case, the main recirculation eddy forms at a large distance from the plate ($x = 9H$).

For the $G/H > 0$, part of the incoming flow is diverted into the bottom gap, where the flow acceleration is large for relatively small bottom gaps [e.g., see Fig. 13(b) for $G/H = 0.1$]. Though the bottom SSL curves toward the top SSL, as also observed for solid plates with small G/H, its effect on the dynamics of the eddies shed in the top SSL is small for $G/H < 0.3$. The relatively strong bleeding flow in between the two SSLs impedes their interactions in the $P = 36\%$ cases. The vortical flow structure changes qualitatively as G/H is increased to 0.5. The upstream part of the bottom SSL is no longer in contact with the channel bottom. Though no clearly defined wake billows form from eddies shed in the bottom SSL, the top and bottom SSLs interact around $x = 8H$ [Fig. 13(c)]. The wake flow behind the plate starts resembling that of the flow past a porous bluff body with $G/H \gg 1$, in which the lengths of the two SSLs are increasing monotonically with the bluff body porosity [31]. The billows advected inside the bottom SSL start interacting with the channel bottom around $x/H = 4$. The coherence of these billows decays fairly rapidly via vortex stretching. No large billows originating in the bottom SSL are observed for $x/H > 12$. For even larger bottom gaps (e.g., $P = 36\%$ $G = 1H$ case), the antisymmetric wake shedding is much stronger [Fig. 13(d)]. Wake billows form around $x = 5H$. By comparison, such billows were generated around $x = 1.5H$ in the corresponding solid plate case [Fig. 5(d)]. This is simply an effect of the bleeding flow [31]. In the $P = 36\%$ $G = 1H$ case, the wake billows originating in the bottom SSL start interacting with the channel bottom around $x/H = 7$ and lose most of the coherence before reaching $x = 16H$. The mechanism responsible for the loss of coherence of the bottom SSL billows is essentially the same as that observed in the $P = 0\%$ $G = 1H$ case.

For cases with $G/H < 0.3$, elongated patches of positive and negative spanwise velocity generated mainly by the passage of the large billows from the top SSL are present in the instantaneous velocity fields [e.g., see Figs. 13(a) and 13(b)]. Compared to the corresponding solid plate cases (Fig. 5), the magnitude of the spanwise velocity inside these patches is smaller by about 30% and the patches form at a larger distance from the plate [e.g., for $x/H > 8$ in Figs. 13(a) and 13(b)]. For $G/H > 0.3$ [Figs. 13(c) and 13(d)], the average velocity magnitude inside these patches does not increase. This suggests that for porous plates with $G/H > 0.3$, the momentum transport in the spanwise direction does not vary significantly with G/H.

For all $P = 36\%$ cases, the velocity power spectra at locations situated close to the origin of the top SSL [point P1 in Fig. 13(a)] contain a band of relatively high frequencies associated with the formation of the first vortex tubes (see spectra at point P1 in Fig. 14). The dominant frequency associated with the passage of the vortex tubes varies little between $G = 0H$ ($\mathrm{St} = 0.75$) and $G = 1H$ ($\mathrm{St} = 0.81$), but the energy associated with the dominant frequency increases significantly with increasing G/H once the antisymmetric wake vortex shedding starts. For $G/H < 0.3$, there is little variation in the value of the Strouhal number associated with the passage of the large billows forming in the top SSL downstream of the main recirculation bubble (e.g., $\mathrm{St} = 0.095$–0.1 for the velocity spectra at point P2 situated at $x = 22H$). As opposed to what was observed for solid plates, no significant change is observed in the dominant passage frequency of the large billows in the top SSL in the $P = 36\%$ $G = 0.1H$ case compared to the $P = 36\%$ $G = 0H$ case. This is because the bleeding flow significantly reduces the interactions between the bottom and top SSLs for small G/H values. Similar to what was observed for solid plates with $G/H \geqslant 0.5$ (see Table I), the Strouhal

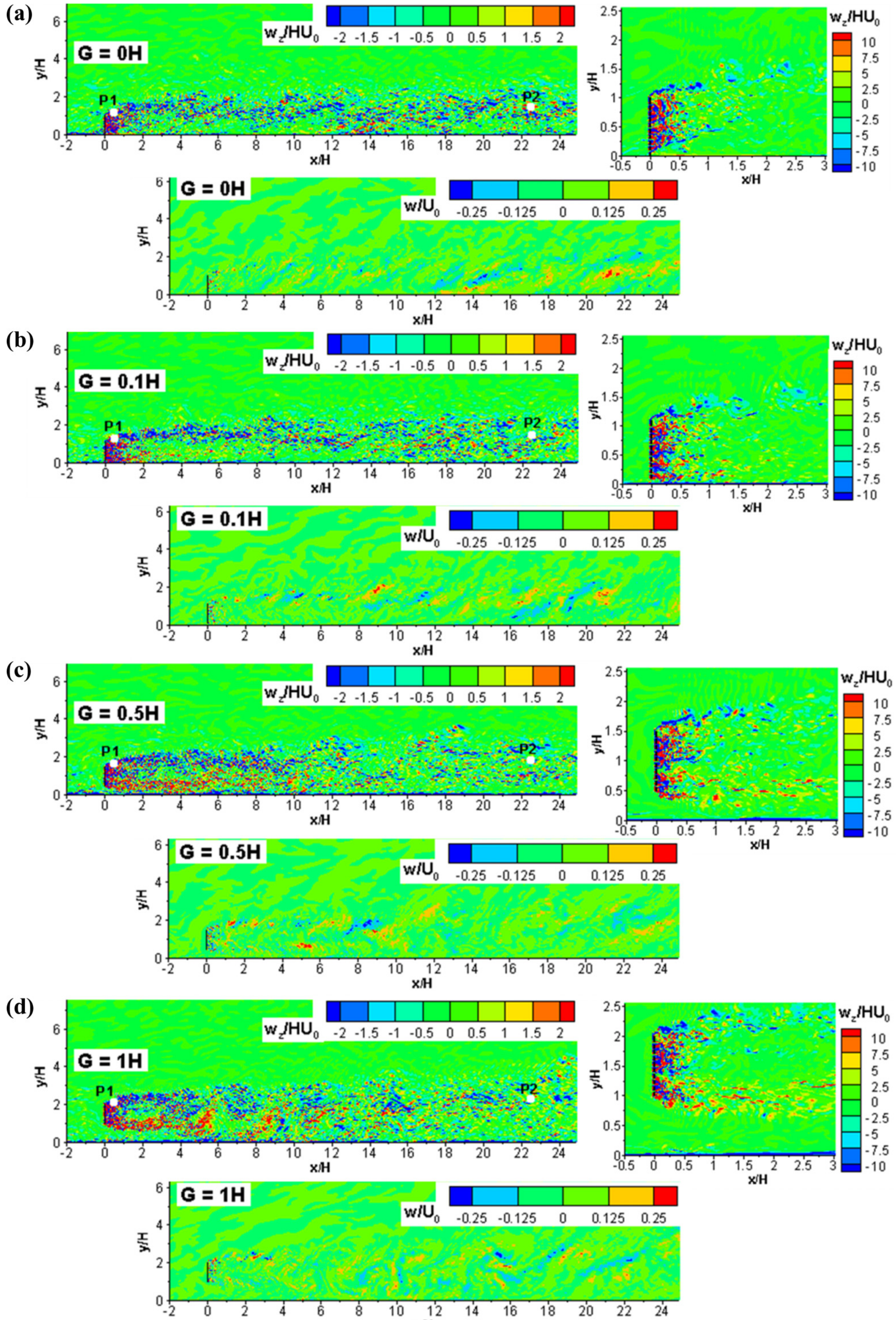

FIG. 13. Instantaneous spanwise vorticity, $\omega_z/(H/U_0)$, and spanwise velocity, w/U_0, in an x-y plane for the porous plate ($P = 36\%$) cases. (a) $G = 0H$; (b) $G = 0.1H$; (c) $G = 0.5H$; (d) $G = 1.0H$.

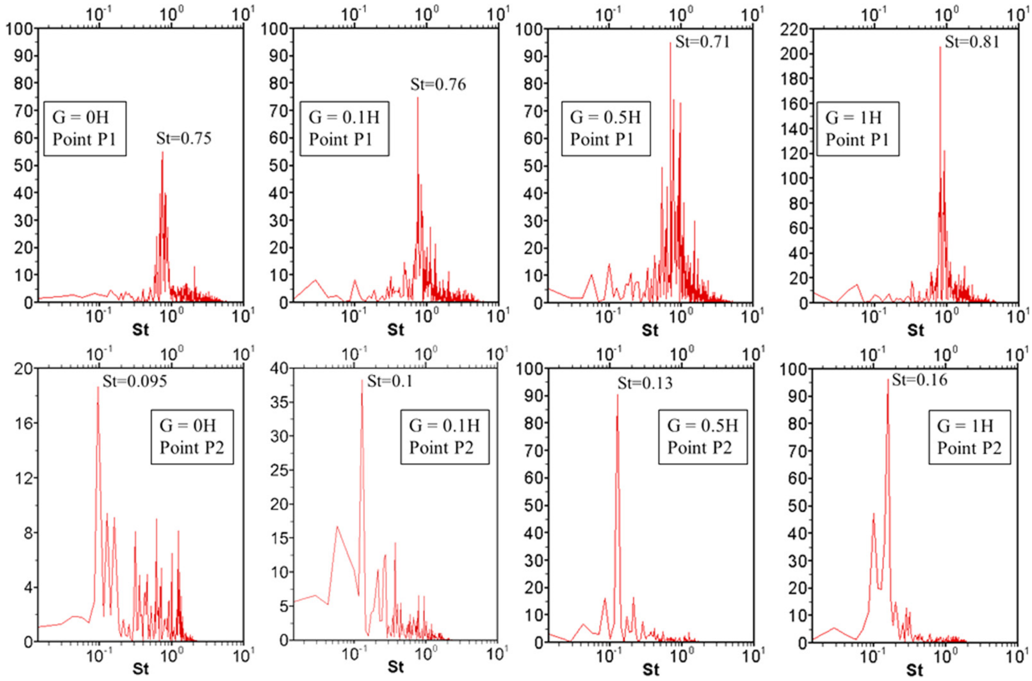

FIG. 14. Power spectra of the vertical velocity at point P1 and point P2 for the porous plate ($P = 36\%$) cases. The positions of points P1 and P2 are shown in Fig. 13. The power spectra are compared for the $G = 0H$, $G = 0.1H$, $G = 0.5H$, and $G = 1.0H$ cases.

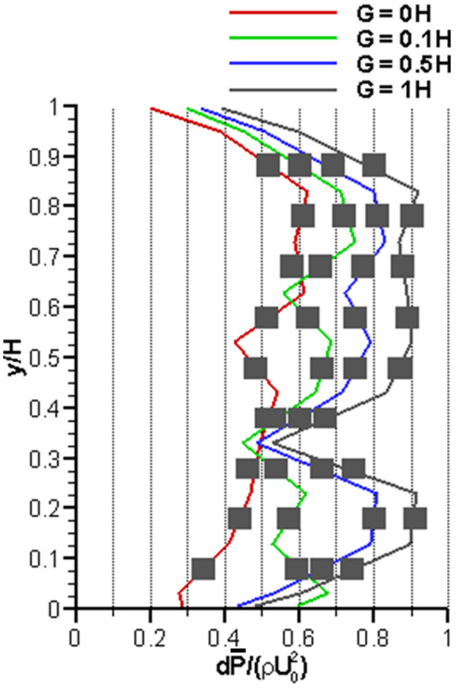

FIG. 15. Spanwise- and time-averaged net pressure distribution on the plate for the porous plate ($P = 36\%$) cases, where y/H represents the vertical distance from the bottom edge of the plate. The gray rectangles indicate the position of the openings between the solid elements.

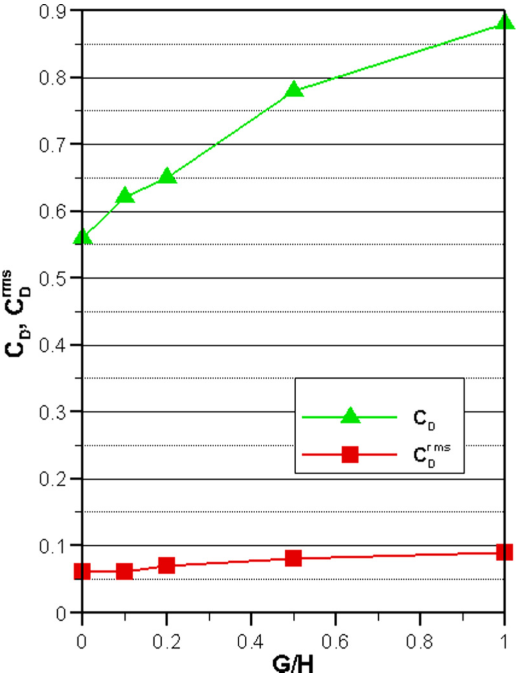

FIG. 16. Effect of varying the bottom gap, G/H, on the mean drag coefficient and the rms fluctuations of the drag coefficient for the porous plate ($P = 36\%$) cases.

number associated with the antisymmetric wake vortex shedding increases with increasing G/H ($\mathrm{St_w} = 0.13$ for $G = 0.5H$ and $\mathrm{St_w} = 0.16$ for $G = 1.0H$). The $\mathrm{St_w}$ value in the $P = 36\%$ $G = 1H$ case is slightly larger than the one predicted in the $P = 0\%$ $G = 1H$ case ($\mathrm{St_w} = 0.14$) and for solid plates with $G/H \gg 1$ ($\mathrm{St_w} = 0.14$–0.15).

C. Forces acting on the plate

For the porous plate cases, the width-averaged net mean pressure distributions on the plate (Fig. 15) show qualitative differences as G/H increases. For $G/H = 0$, the maximum value of the net pressure is observed close to the top part of the plate. The net pressure decays in a nonmonotonic way as the bottom edge of the plate is approached. In the cases with $G/H > 0$, the net pressure also peaks close to the top edge of the porous plate. It then remains approximatively constant in the region where the bleeding flow is advected toward the top SSL before decaying sharply around the location where the second recirculation bubble touches the back of the porous plate. The net pressure increases again in the region where the bleeding flow is advected toward the bottom layer before decaying again in the vicinity of the bottom edge of the plate.

Similar to the $P = 0\%$ cases, an overall increase of the net pressure acting on the plate is observed with increasing G/H. This also translates into a monotonic increase of the mean drag coefficient,$\bar{C}_{\mathrm{D}}$, with increasing G/H (Fig. 16). The increase of the rms of the drag coefficient fluctuations, C_D^{rms}, is due to the increase of the interactions between the top and bottom SSLs and the onset of antisymmetric shedding for $G/H \geqslant 0.5$. For the same G/H, the values of $\bar{C}_{\mathrm{D}}$ are smaller in the porous plate simulations (Table II) compared to the solid plate simulations (Table I). For $G/H < 0.5$, C_D^{rms} is larger in porous plate simulations due to the turbulence generated by the jets forming in between the solid elements of the plate. For $G/H \geqslant 0.5$, C_D^{rms} is larger in the solid plate simulations. This is because the main contributor to the oscillations of the drag coefficient is the

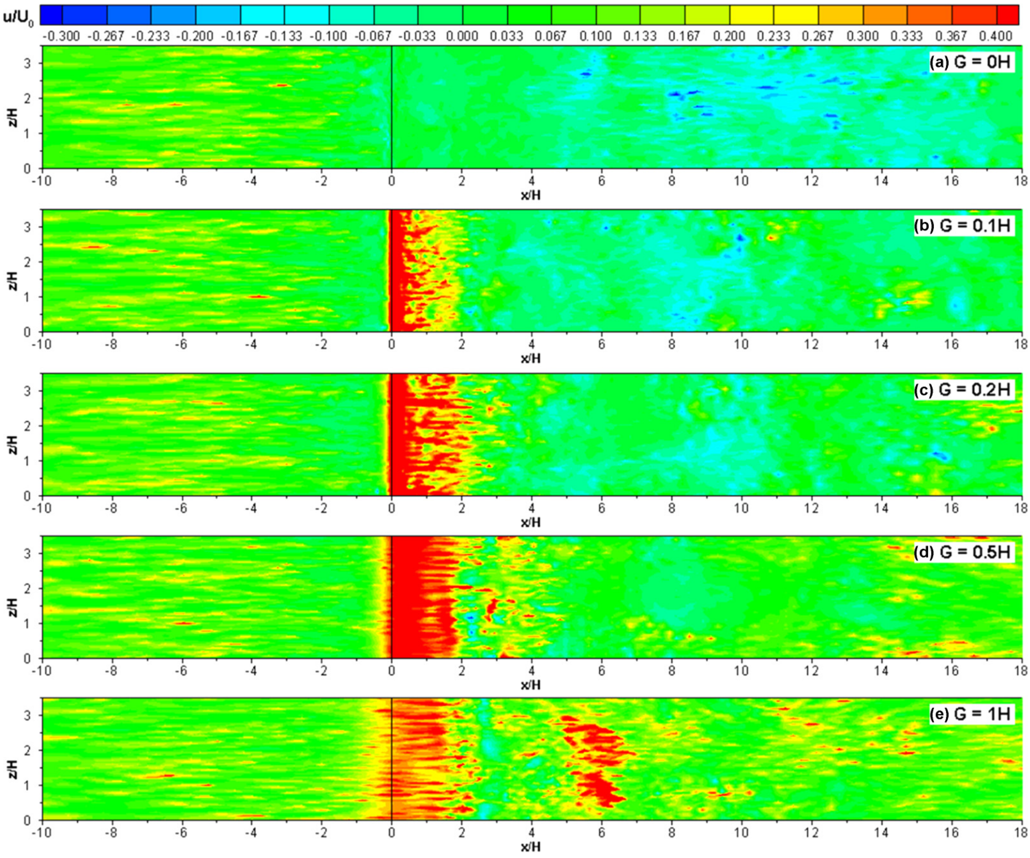

FIG. 17. Instantaneous streamwise velocity, u/U_0, distribution on a horizontal plane situated at a distance of $0.0055H$ from the bottom surface for the porous plate ($P = 36\%$) cases. (a) $G = 0H$; (b) $G = 0.1H$; (c) $G = 0.2H$; (d) $G = 0.5H$; (e) $G = 1.0H$.

advection of billow vortices. These billow vortices are more coherent and form closer to the plate for low porosity plates.

D. Bed friction velocity

As for the solid plate cases, the flow advected through the bottom gap leads to a significant amplification of the near-bed streamwise velocity and thus of the bed friction velocity beneath the plate and over some distance from it (Fig. 17). For $G/H \geqslant 0.2$, the streamwise velocity streaks behind the plate are not destroyed. For $G/H \geqslant 0.5$, the near-bed flow is accelerated or decelerated due to the wake billows originating in the bottom SSL.

For $G/H > 0$, the mean bed friction velocity magnitude, $u_\tau/u_{\tau 0}$, is strongly amplified beneath the porous plate as the flow passing the gap region accelerates. The values of $u_\tau/u_{\tau 0}$ predicted beneath the gate in the $P = 36\%$ cases are 30–60% lower than those predicted for solid plates [Figs. 9(a) and 18(a)]. This is because the part of the incoming flow approaching the upstream face of the plate that is diverted beneath its bottom edge is always smaller in the case of a porous plate. In the $P = 36\%$ cases with $G/H > 0$, a region of nonmonotonic decay toward a minimum value that is less than $u_{\tau 0}$ is present in Fig. 18(a). The distance between the plate and the location of the minimum of $u_\tau/u_{\tau 0}$ is the largest for $G/H = 0.5$ ($\approx 22H$), where the wake billows form at the largest distance from the plate.

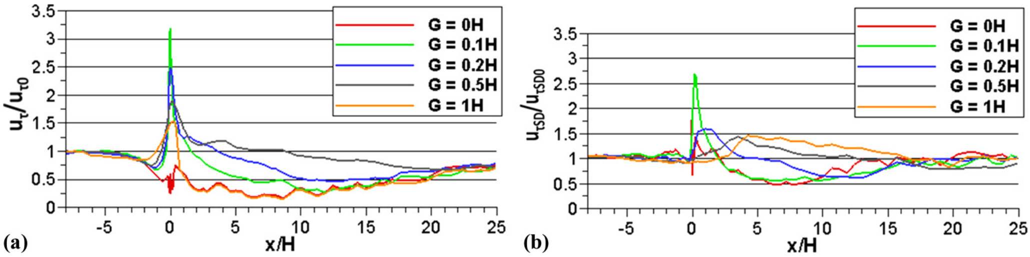

FIG. 18. Effect of G/H on the (a) nondimensional, spanwise-averaged bed friction velocity magnitude in the mean flow and (b) nondimensional rms fluctuations of the bed friction velocity, $u_{\tau\mathrm{SD}}$, for the porous plate ($P = 36\%$) cases.

The distributions of $u_{\tau SD}/u_{\tau\mathrm{SD}0}$ in Fig. 18(b) are qualitatively different in the $G/H > 0$ cases with and without antisymmetric wake vortex shedding. In the former cases, $u_{\tau\mathrm{SD}}$ is strongly amplified beneath the porous plate and then decreases fairly rapidly until $x = 8H$–$11H$ before starting to recover toward the value corresponding to fully developed channel flow, which is reached around $x = 20H$. In the cases where vortex shedding is present, there is no amplification of $u_{\tau\mathrm{SD}}$ beneath the plate. Rather $u_{\tau\mathrm{SD}}$ increases to about $1.5u_{\tau\mathrm{SD}0}$ around $x = 5H$. Downstream of this location, $u_{\tau\mathrm{SD}}$ starts decaying slowly and approaches $u_{\tau\mathrm{SD}0}$ around the location where the wake billows advected in the bottom SSL have lost most of their coherence (e.g., $x \approx 16H$ for the $P = 36\%$ $G = 1H$ case).

VI. SUMMARY AND CONCLUSIONS

High-resolution, three-dimensional LES were used to study how the physics of turbulent flow past a thin plate situated in the vicinity of a solid, no-slip boundary changes as a function of the bottom gap ratio for $0 \leqslant G/H \leqslant 1$ for both solid plates ($P = 0\%$) and porous plates with $P = 36\%$. Analysis of the 3D flow fields clarified how the wake structure gradually approaches the canonical case of flow past a solid plate with $G/H \gg 1$.

In the $P = 0\%$ cases with $G/H \leqslant 0.2$, a recirculation bubble formed in between the plate and the channel bottom, while for $G/H \geqslant 0.5$, a separation bubble containing two eddies formed at the back of the plate, similar to cases with $G/H \gg 1$. Even for cases with relatively small G/H values, the bottom SSL had a strong effect on the coherence of the large-scale billows forming in the top SSL. In simulations where a recirculation bubble formed and $G/H > 0$, a merging event occurred between successively shed billows inside the top SSL before these billows were advected past the end of the bottom-attached recirculation bubble. Thus, the dominant frequency in the wake past the reattachment location was two times lower than the frequency of passage of the large billows in the downstream part of the top SSL.

In the $P = 36\%$ cases, no bottom-attached recirculation bubbles were present except for $G/H = 0$, where a small recirculation bubble formed away from the plate. Meanwhile, several recirculation eddies formed at the back of the porous plate. The main recirculation eddy touched the back of the plate at the location where the bleeding flow splits into two components that are advected toward the top and bottom SSLs, respectively. Due to the bleeding flow, the natural interaction of the two SSLs was impeded close to the porous plate. This explains the much larger length of the SSLs observed for large G/H in the porous plate cases compared to the corresponding solid plate cases.

For both solid and porous plates, there is a threshold value of G/H for which the wake structure changes from a wake containing mainly corotating vortices originating in the top SSL to a wake containing counter-rotating billow vortices generated by the interaction of the top and bottom SSLs. This value is close to 0.5 for plates with $P = 36\%$ and slightly smaller for plates with $P = 0\%$. Once the antisymmetric wake shedding is present, the Strouhal number associated with the shedding of counter-rotating wake vortices was found to increase with increasing G/H for both solid and porous plates. For solid plates, the shedding frequency predicted for $G/H = 1$ was very close to the value expected for solid plates with $G/H \gg 1$. For the same G/H, the Strouhal number corresponding to the shedding frequency was slightly higher in the $P = 36\%$ cases compared to the $P = 0\%$ cases. For both solid and porous plate cases with antisymmetric wake vortex shedding, the coherence of the billows shed from the top and bottom SSLs was initially comparable. Once the billows originating in the bottom SSL approached the channel bottom, their streamwise advection was slowed down and their coherence decayed rapidly due to interactions with the large billows originating from the top SSL.

For both solid and porous plates, the mean drag coefficient and its rms fluctuations increased monotonically with increasing G/H. Even for solid plates with $G/H = 1$ the effect of the bottom gap was not negligible, as the predicted value of the drag coefficient was about 25% smaller than the one expected for solid plates with $G/H \gg 1$. For the same G/H, the predicted mean drag coefficient was smaller in the porous plate case, an effect associated with the bleeding flow.

For plates with $G/H \geqslant 0.1$, the flow advected through the bottom gap induced a strong increase of the bed friction velocity and its rms fluctuations around the plate location. The increase in the rms fluctuations of the bed friction velocity at locations situated downstream of the plate is mostly related to eddies generated in the bottom SSL that approach the channel bottom. There is no clear trend in terms of how the total particle entrainment capacity of the flow varies with increasing G/H for solid plates positioned above a loose bed. For porous plates with $P = 36\%$, simulation results suggest that the total particle entrainment capacity of the flow behind the plate peaks around $G/H = 0.5$, where high values are predicted for both the mean bed friction velocity and its rms fluctuations, and is the smallest for small values of G/H.

At a more general level, information obtained from simulations containing a porous plate contributed to enhancing the general understanding of the effect of installing wind barriers offering protection against hurricanes, barriers controlling Aeolian sand transport in arid and coastal regions, and snow fences used to reduce snow drifting on roads. Such an understanding is a prerequisite toward developing methods to control particulate dynamics in the vicinity of these structures. Another issue that has to be addressed is that of scale effects between laboratory and field conditions. Hybrid RANS-LES approaches such as detached eddy simulation [20] offer an alternative to LES to conduct high-resolution simulations at field-scale conditions that can be used to investigate scale effects for practical applications.

ACKNOWLEDGMENTS

This work was partially supported by the Iowa Department of Transportation Project No. IHRB 10-02 (Iowa Highway Research Board). We gratefully acknowledge the National Center for High Performance Computing (NCHC) in Taiwan, in particular Dr. W. F. Tsai, for providing substantial computer time to perform the simulations.

---

[1] A. M. Hamed, and L. P. Chamorro, Turbulent boundary layer around 2D permeable and impermeable obstacles, Exp. Fluids **59**, 134 (2018).

[2] Z. Dong, W. Luo, G. Qian, P. Lu, and H. Wang, A wind tunnel simulation of the turbulence fields behind upright porous wind fences, J. Arid. Environ. **74**, 193 (2010).

[3] A. M. Saif, A. M. I. Mohamed, and A. M. Alam Eldein, Variable porosity wind fences to control aeolian sand transport, CD-ROM *Proceedings of Tenth International Congress of Fluid Dynamics ICFD10-EG-3090* (ICFD10, Ain Soukna, Egypt, 2010).

[4] X. C. Cong, S. Q. Cao, Z. L. Chen, S. T. Peng, and S. L. Yang, Impact of the installation scenario of porous fences on wind-blown particle emission in open coal yards, J. Atmos. Environ. **45**, 5247 (2011).

[5] K. Basnet, M. Muste, G. Constantinescu, H. Ho, and H. Xu, Close range photogrammetry for dynamically tracking drifted snow deposition, Cold Reg. Sci. Technol. **121**, 141 (2016).

[6] K. Basnet, G. Constantinescu, M. Muste, and H. Ho, Method to assess efficiency and improve design of snow fences, ASCE J. Eng. Mech. **141**, 04014136 (2015).

[7] M. D. Perera, Shelter behind two-dimensional solid and porous fences, J. Wind Eng. Ind. Aerodyn. **8**, 93 (1981).

[8] A. R. Borges and D. X. Viegas, Shelter effects on a row of coal piles to prevent wind erosion, J. Wind Eng. Ind. Aerodyn. **29**, 145 (1988).

[9] S. C. Yaragal, H. S. Govinda Ram, and K. K. Murthy, Two-dimensional flow field behind perforated plates on a flat surface, J. Wind Eng. and Industrial Aerodynamics **90**, 75 (2002).

[10] S. J. Lee and H. B. Kim, Velocity field measurements of flow around a triangular prism behind a porous fence, J. Wind Eng. Ind. Aerodyn. **77-78**, 521 (1998).

[11] H. Haniu, H. Sakamoto, and K. Takai, Improvement of blower type snow fences by control of the shear layer, J. Nat. Disaster Sci. **17**, 53 (1995).

[12] Z. Dong, W. Luo, G. Qian, and H. Wang, A wind tunnel simulation of the mean velocity fields behind upright porous fences, Agric. For. Meteorol. **146**, 82 (2007).

[13] I. P. Castro, Wake characteristics of two-dimensional perforated plates normal to an air-stream, J. Fluid Mech. **46**, 599 (1971).

[14] S. J. Lee and H. B. Kim, Laboratory measurements of velocity and turbulence field behind porous fences, J. Wind Eng. Ind. Aerodyn. **80**, 311 (1999).

[15] K. G. Rangaraju, R. J. Garde, S. K. Singh, and N. Singh, Experimental study on characteristics of flow past porous fences, J. Wind Eng. Ind. Aerodyn. **29**, 155 (1988).

[16] J. D. Wilson, A field study of the mean pressure about a windbreak, Boundary Layer Meteorol. **85**, 327 (1997).

[17] S. J. Lee and H. C. Lim, A numerical study on flow around a triangular prism located behind a porous fence, Fluid Dyn. Res. **28**, 209 (2001).

[18] J. L. Santiago, F. Martin, A. Cuerva, N. Bezdenejnykh, and A. Sanz-Andres, Experimental and numerical study of wind flow behind windbreaks, Atmos. Environ. **41**, 6406 (2007).

[19] L.-M. Huang, H. C. Chan, and J.-T. Lee, A numerical study of flow around nonuniform porous fences, J. Appl. Math. **2012**, 268371 (2012).

[20] W. Rodi, G. Constantinescu, and T. Stoesser, Large-Eddy Simulation in Hydraulics, *IAHR Monograph* (CRC Press, Taylor & Francis, Oxfordshire, UK, 2013).

[21] K. Basnet and G. Constantinescu, The structure of flow around a porous plate attached to a horizontal bed, Phys. Fluids **29**, 115101 (2017).

[22] D. F. G. Durao, M. V. Heitor, and J. C. F. Pereira, Measurements of turbulent and periodic flows around a square cross-section cylinder, Exp. Fluids **6**, 298 (1988).

[23] G. Bosch, M. Kappler, and W. Rodi, Experiments on the flow past a square cylinder placed near a wall, J. Exp. Thermal Fluid Sci. **13**, 292 (1996).

[24] R. J. Martinuzzi, S. C. C. Bailey, and G. A. Kopp, Influence of wall proximity on vortex shedding from a square cylinder, Exp. Fluids **34**, 585 (2003).

[25] P. K. Panigrahi, PIV investigation of flow behind surface mounted detached square cylinder, J. Fluids Eng. **131**, 011202 (2009).

[26] H. M. Cho, Wind-tunnel and numerical simulation of flow over porous fences and particle saltation in atmospheric boundary layer, Ph.D. dissertation, Department of Mechanical and Aeronautical Engineering, University of California at Davis, 1996.

[27] F. M. Najjar and S. P. Vanka, Numerical study of a separated-reattaching flow, Theor. Comput. Fluid Dyn. **5**, 291 (1993).

[28] H. B. Kim and S. J. Lee, The structure of turbulent shear flow around a two-dimensional porous fence having a bottom gap, J. Fluids Struct. **16**, 317 (2002).

[29] F. M. Fang and D. Y. Wang, On the flow around a vertical porous fence, J. Wind Eng. Ind. Aerodyn. **67-68**, 415 (1997).

[30] J. Zhou, C. Cenedese, T. Williams, M. Ball, S. Venayagamoorthy, and R. Nokes, On the propagation of gravity currents over and through a submerged array of circular cylinders, J. Fluid Mech. **831**, 394 (2017).

[31] K. S. Chang and G. Constantinescu, Numerical investigation of flow and turbulence structure through and around a circular array of rigid cylinders, J. Fluid Mech. **776**, 161 (2015).

[32] C. D. Pierce and P. Moin, Progress-variable approach for large-eddy simulation of turbulent combustion, Mech. Eng. Dept.Report No. TF-80, Stanford University (2001).

[33] K. Mahesh, S. G. Constantinescu, and P. Moin, A numerical method for large eddy simulation in complex geometries, J. Comput. Phys. **197**, 215 (2004).

[34] K. Chang, G. Constantinescu, and S. O. Park, Analysis of the flow and mass transfer process for the incompressible flow past an open cavity with a laminar and a fully turbulent incoming boundary layer, J. Fluid Mech. **561**, 113 (2006).

[35] E. Gonzales-Juez, E. Meiburg, and G. Constantinescu, Gravity currents impinging on bottom-mounted square cylinders: Flow fields and associated forces, J. Fluid Mech. **631**, 65 (2009).

[36] K. S. Chang and G. Constantinescu, Coherent structures in developing flow over 2D dunes, Water Resour. Res. **49**, 2446 (2013).

[37] T. Tokyay, G. Constantinescu, and E. Meiburg, Lock exchange gravity currents with a low volume of release propagating over an array of obstacles, J. Geophys. Res. Oceans **119**, 2752 (2014).

[38] T. Tokyay and G. Constantinescu, The effects of a submerged non-erodible triangular obstacle on bottom propagating gravity currents, Phys. Fluids **27**, 056601 (2015).

[39] A. Yuksel-Ozan, G. Constantinescu, and H. Nepf, Free surface gravity currents propagating in an open channel containing a porous layer at the free surface, J. Fluid Mech. **809**, 601 (2016).

[40] K. S. Chang and G. Constantinescu, 2D eddy resolving simulations of flow past a circular patch of cylinders, J. Hydrodynam. B **30**, 317 (2018).

[41] E. Gonzales-Juez, E. Meiburg, T. Tokyay, and G. Constantinescu, Gravity current flow past a circular cylinder: forces, wall shear stresses and implications for scour, J. Fluid Mech. **649**, 69 (2010).

[42] D. A. Lyn, S. Einav, W. Rodi, and J. H. Park, A laser-Doppler velocimetry study of ensemble-averaged characteristics of the turbulent near wake of a square cylinder, J. Fluid Mech. **304**, 285 (1995).

[43] G. Wang and S. P. Vanka, Large-eddy simulations of high Reynolds number turbulent flow over a square cylinder, Department of Mechanical and Industrial Engineering Report No. CFD 96-02, University of Illinois at Urbana-Champaign, IL (1996).

[44] Y. Srinivas, G. Biswas, A. S. Parihar, and R. Ranjan, Large-eddy simulation of high Reynolds number turbulent flow past a square cylinder, J. Eng. Mech. **132**, 327 (2006).

[45] M. Kiya and M. Matsumura, Incoherent turbulence structure in the near wake of a normal plate, J. Fluid Mech. **190**, 343 (1988).

[46] A. Fage and F. C. Johansen, On the flow of air behind an inclined flat plate of infinite span, Proc. R. Soc. London A **116**, 170 (1927).